Article

Synthesis and Comprehensive Analytical Study of β-Li$_3$PS$_4$ Stabilization by Ca- and Ba-Codoped Li$_3$PS$_4$

Fuki Baba, Futoshi Utsuno, and Takahiro Ohkubo*

Read Online

ACCESS | Metrics & More | Article Recommendations | Supporting Information

ABSTRACT: Sulfide-based solid electrolytes with high Li$^+$ conductivity, such as Li$_3$PS$_4$, are key materials for the realization of all-solid-state Li$^+$ batteries. One approach to achieving high Li$^+$ conductivity is to combine crystalline-phase stabilization at high temperatures with the introduction of defects at room temperature. In this work, this approach was verified by codoping Li$_3$PS$_4$ with two kinds of divalent cations. The resulting structural changes were comprehensively investigated both experimentally and computationally. The high-temperature β-Li$_3$PS$_4$ phase of Li$_3$PS$_4$ could be stabilized at room temperature by adjusting the amount of Ca or Ba doping. The synthesized samples doped with divalent cations were found to have conductivities about 2 orders of magnitude higher than that of the γ-Li$_3$PS$_4$ phase at room temperature. The resultant Li$^+$ conductivity at room temperature was also higher than that expected from interpolation of results for nondoped β-Li$_3$PS$_4$. It is believed that the structural changes produced by the divalent cation doping contribute to this increase in conductivity. The stability of the β-Li$_3$PS$_4$ phase with divalent cation doping was also demonstrated using density-functional-theory calculations for models with equivalent compositions to the synthesized samples. The Li$^+$ positions obtained by structural optimization calculations showed the presence of diverse and disordered Li sites in the Ca-doped lattice. Such structural changes can contribute to cascade processes involving Li$^+$ collisions, referred to as the "billiard-ball" mechanism, which cannot occur in nondoped β-Li$_3$PS$_4$. This series of experiments involving the synthesis and analyses of β-Li$_3$PS$_4$ with divalent cation doping provides a way to enhance Li$^+$ conductivity through structural modification and optimization.
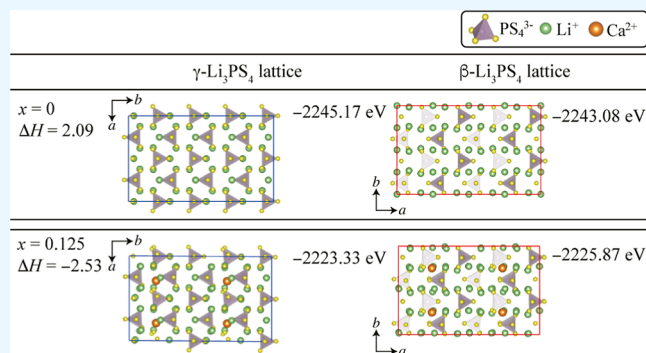
1. INTRODUCTION

All-solid-state rechargeable Li$^+$ batteries using solid-state electrolytes instead of organic liquid electrolytes have been widely studied in recent years with a view to their practical use.[1−3] They are considered to be capable of achieving high energy density without the risk of the leakage of liquid electrolytes and ignition in harsh environments, such as when subjected to high temperatures or mechanical deformation.[4−8]

Current solid electrolytes for all-solid-state Li$^+$ batteries can be roughly classified into oxide and sulfide compounds. Oxide-based solid electrolytes have excellent atmospheric stability. Typical crystalline compounds are NASICON,[9,10] perovskite,[11,12] LISICON,[13,14] and garnet crystals.[15] However, sulfide-based solid electrolytes are also promising candidates for practical use because of their superior Li$^+$ conductivity and the fact that they form an electrode interface with better contact properties than oxide-based solid electrolytes.[16,17] The argyrodite-type solid electrolyte Li$_7$PS$_6$, which is a material exhibiting high Li$^+$ conductivity, has been found to exhibit a conductivity of 10^{-4} S cm^{-1} at room temperature.[18] Furthermore, the conductivity of this material was improved to 10^{-2} S cm^{-1} by the substitution of halogen anions X (X = Cl and Br) for S^{2-} at 4a and 4c sites in Li$_7$PS$_6$.[19] Efficient

conduction paths are formed by structural disorder due to this halogen substitution. This improvement of ionic conductivity based on atomic substitution is an important concept for designing electrolytes to improve their conductivity.[20]

Currently, two approaches have been proposed for the structural modification of crystalline materials to improve their ionic conductivities at room temperature. The first approach is to stabilize the high-temperature phase at room temperature, which has a relatively disordered structure involving open voids for ionic conduction. A typical crystalline compound for this concept is β-alumina solid electrolyte, in which the disordered structure can exhibit nonstoichiometric behavior and contain a large excess of mobile ions in the ionic conduction space.[21] Stabilization of the high-temperature phase has generally been achieved by doping with impurities

and creating multiphase composites such as glassy and crystalline states. These modifications can result in high entropy and lead to stabilization of the high-temperature phase at room temperature. Improvements in stabilizing high-temperature phases at room temperature have also been reported for sulfides. γ-Phase Li_3PS_4 (γ-Li_3PS_4; space group $Pmn2_1$) is a stable crystal in the $Li_2S-P_2S_5$ system at room temperature. The phase transition from γ-Li_3PS_4 to the β phase (β-Li_3PS_4; space group $Pnma$) occurs at 573 K.[22,23] Stabilized β-Li_3PS_4 including amorphous phases with nanoporous interference at room temperature has been obtained via liquid-phase synthesis.[24] This compound was found to exhibit a dramatically high Li^+ conductivity of about 10^{-4} S cm^{-1}[25,26] when compared to that of γ-Li_3PS_4 at room temperature (10^{-6} S cm^{-1}).

The second approach to improving the conductivity of these materials is the introduction of explicit vacancies for Li^+ conduction by doping with multivalent cations instead of Li^+.[26–30] Substitution of Li^+ for a divalent cation can produce a vacancy site for charge neutrality. An increase in conductivity based on this concept has been reported for Na^+ solid-state electrolytes (Na_3PS_4), in which some Na^+ are replaced by Ca^{2+}.[31]

In this study, solid-state Ca- and Ba-doped Li_3PS_4 crystals were newly synthesized based on the concepts of the two approaches described above. The stabilization of the high-temperature β-Li_3PS_4 phases and the introduction of vacancies for Li^+ conduction were studied to enhance the Li^+ conductivity at room temperature. The changes in the crystalline lattice and the local structure of the PS units (PS_4^{3-}, $P_2S_6^{4-}$, and $P_2S_7^{4-}$) were comprehensively identified by powder X-ray diffraction (XRD) measurements and ^{31}P nuclear magnetic resonance (NMR) spectroscopy. Theoretical verification of the synthesized Ca-doped Li_3PS_4 crystals was also performed by using ab initio calculations.

2. EXPERIMENTAL SECTION

2.1. Synthesis. Herein, Ca- and Ba-doped Li_3PS_4 are denoted as $Li_{3-2x}Ca_xPS_4$ and $Li_{2.9}Ca_yBa_{0.05-y}PS_4$, where x and y are 0, 0.0250, 0.0375, 0.0500, 0.1000, and 0.1500 and 0, 0.005, 0.015, 0.025, 0.035, and 0.045, respectively. The starting materials to synthesize $Li_{3-2x}Ca_xPS_4$ and $Li_{2.9}Ca_yBa_{0.05-y}PS_4$ were Li_2S (Idemitsu Kosan Co., Ltd., >99.9%), P_2S_5 (Sigma-Aldrich, 99.8%), CaS (Kojundo Chemical Laboratory Co., Ltd., 99.9%), and BaS (Kojundo Chemical Laboratory Co., Ltd., 99.9%). These starting materials were weighed in the targeted stoichiometric ratios (total mass = 3.5 g) and mixed by using an agate mortar and pestle for 5 min. The mixed powder was transferred into a ZrO_2 ball-milling pot (45 mL) with ZrO_2 balls (ϕ = 5 mm, 56 g). These operations were performed in Ar-filled gloveboxes with a dew point below 80 °C (Glovebox Japan Inc.).

Mechanical milling using a Fritsch Pulverisette 7 Premium line was undertaken for 40 cycles, in which one cycle was composed of 60 min of milling (370 rpm) and 5 min of rest. The direction of rotation was also reversed for each cycle. After this mechanical milling treatment, the mixture was collected and pelletized using a hydraulic press and a stainless-steel mold in a glovebox. These pellets were transferred into a quartz tube in the glovebox. The quartz tube was connected to the vacuum line and sealed under vacuum at 0.1 Pa. The sealed pellets were heated to 823 K for 48 h and allowed to cool to room temperature naturally. The sample powder was collected by

breaking the quartz tube in the glovebox for subsequent measurements.

2.2. Powder XRD. XRD measurements were performed using an M03XRF diffractometer (MAC Science Co., Ltd.) equipped with a Si monochromator with Cu Kα radiation (λ = 1.5418 Å) at 40 kV and 40 mA. The powder sample was mounted in a glass sample holder and sealed with Kapton polyimide film and NITOFLON tape to prevent any reaction with moisture and oxygen in the air. Diffraction data were collected within the range of 10–60° at room temperature. The Profex software package[32] for Rietveld refinement was used to evaluate the lattice constants from the diffraction data. The XRD patterns obtained from the synthesized samples consist of unknown crystalline multiple phases, as described later. Additionally, the use of Kapton films results in broad background peaks. Consequently, determining all crystalline parameters such as atomic occupancy proves to be challenging. Therefore, Rietveld analysis in this study was employed solely to determine the lattice parameters for doped single β-Li_3PS_4 phases within the data range of 12–21°, where the peaks originating from the β phase are exclusively observed. In other words, the fitting range was restricted to data ranging from 12 to 21°, and the Ca/Li occupancy was fixed at the value expected from the composition.

2.3. Solid-State NMR Spectroscopy. ^{31}P magic-angle spinning (MAS) NMR spectroscopy using dry air was performed with a JEOL JNM-ECX400 spectrometer (9.4 T) with a 4 mm MAS probe. The ^{31}P MAS NMR spectra were collected at a spinning frequency of 15 kHz with a $\pi/2$ excitation pulse of 3.11 μs. A total of 32 scans with a 60 s recycle delay were used to ensure good quantitative peak intensities. The chemical shifts of the ^{31}P MAS NMR spectra were referenced to an 85% H_3PO_4 solution (0 ppm).

^7Li MAS NMR spectroscopy was performed by using a JEOL JNM-ECZ-600R spectrometer (14.1 T) with a 3.2 mm MAS probe. The ^7Li MAS NMR experiments were performed with a 20 kHz spinning speed and a 2.90 μs excitation pulse. The delay time between each of the eight scans was set to 60 s to ensure good quantitative peak intensities. A 1 M LiCl solution was used for the chemical shift reference (0 ppm).

For the solid-state ^{31}P and ^7Li NMR measurements, the samples were packed into ZrO_2 sample tubes in a glovebox. No spectral changes were observed during the NMR measurements, meaning that the use of airtight sample tubes prevented reactions with oxygen and water in the air.

2.4. Impedance Spectroscopy. Electronic cells including the samples were fabricated in the glovebox. In each case, a powder sample in a poly(ether ether ketone) (PEEK) cylinder was pressed at 360 MPa by uniaxial compression using two stainless-steel rods. Cold pressing was performed three times by turning the PEEK cylinder over. Both sides of each pellet were coated with conductive carbon powder (MCP-15, Nippon Graphite) and pressed at 180 MPa. The cylindrical stainless-steel rods were used as electrodes. Each electronic cell was transferred into an airtight holder, and AC impedance measurements were performed using an impedance analyzer (Solartron, 1260) in the frequency range of 1 Hz to 1 MHz with a N_2 flow. The temperature was controlled from room temperature to 353 K using heated N_2 gas.

3. AB INITIO CALCULATIONS

First-principles density-functional-theory (DFT) calculations were performed using the Vienna ab initio simulation
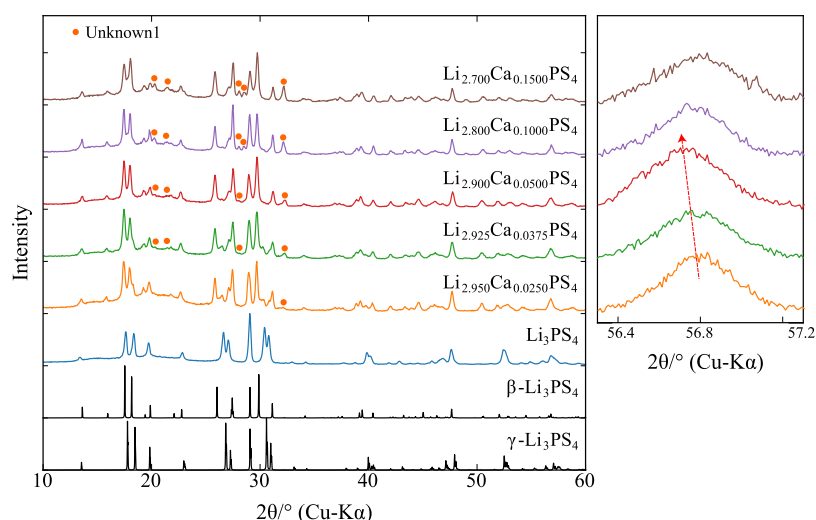
Figure 1. XRD patterns for $Li_{3-2x}Ca_xPS_4$ (x = 0, 0.0250, 0.0375, 0.0500, 0.1000, and 0.1500) and referenced crystalline patterns of γ-Li_3PS_4[23] and β-Li_3PS_4.[40] In the right-hand panel, selected peaks are shown enlarged to highlight their shift with compositional change.

package[33] within the projector augmented-wave method.[34] The generalized gradient approximation using the Perdew–Burke–Ernzerhof revised functional (GGA-PBE) was applied to describe the electron exchange–correlation energy.[35] The cutoff energy for the plane-wave basis was set to 258.7 eV as required by the pseudopotentials. The k-point sampling was distributed within the Brillouin zone in a $1 \times 1 \times 1$ Monkhorst–Pack grid.[36] The convergence criterion for the self-consistent field cycle was set as 1.0×10^{-8} eV in total energy. The DFT-D3 method was also used to correct for van der Waals interactions due to London dispersion forces.[37] The structural optimization was performed until the maximum force in all atoms was less than 2.0×10^{-3} eV/Å.

The initial structures for ab initio calculations were obtained from a $2 \times 4 \times 4$ supercell (512 atoms) of γ-Li_3PS_4 and a $2 \times 2 \times 4$ supercell (512 atoms) of β-Li_3PS_4, which allowed representation of the compositions of the Ca-doped experimental samples in this study. There are three crystallographically equivalent Li sites in β-Li_3PS_4 (8d, 4b, and 4c).[23] The occupancies of the 8d, 4b, and 4c sites in the reported crystalline data are 1.0, 0.7, and 0.3, respectively. Lepley et al. reported that a structure with 4b occupation of Li^+ is the most stable for nondoped β-Li_3PS_4 crystals.[38,39] In accordance with this result, only the 8d and 4b sites were considered for the substitution of Li^+ for Ca. The distances between substitution sites were chosen to be as far apart as possible. The γ-Li_3PS_4 and β-Li_3PS_4 structures corresponding to $Li_{3-2x}Ca_xPS_4$ (x = 0, 0.0156, 0.0312, 0.0625, 0.0938, and 0.1250) were made by replacing two Li^+ with one Ca^{2+} to maintain charge neutrality. The total number of atoms in $Li_{3-2x}Ca_xPS_4$ (x = 0, 0.0156, 0.0312, 0.0625, 0.0938, and 0.1250) was 512, 511, 510, 508, 506, and 504, respectively.

4. RESULTS

4.1. X-ray Diffraction. Figure 1 shows the XRD patterns of $Li_{3-2x}Ca_xPS_4$ (x = 0, 0.0250, 0.0375, 0.0500, 0.1000, and 0.1500) along with the reference patterns of γ-Li_3PS_4[23] and β-Li_3PS_4[40] (first and second from the bottom). The XRD patterns of the reference compounds were calculated from crystalline structure using the diffraction-pattern module in VESTA.[41] The broad background peak ranging from 10 to 25°

was observed for all samples, and this corresponds to the polyimide film used for sealing the samples.

The XRD pattern of Li_3PS_4 without Ca doping shown in Figure 1 (third from the bottom) matches the reference pattern of γ-Li_3PS_4 well. The main peaks of $Li_{3-2x}Ca_xPS_4$ (x = 0.0250, 0.0375, 0.0500, 0.1000, and 0.1500) were assigned to the β-Li_3PS_4 phase (high-temperature phase) at room temperature, meaning that the stabilization of the high-temperature phase at room temperature was achieved with Ca doping. Many diffraction peaks expected from β-Li_3PS_4 and γ-Li_3PS_4 crystals were overlapped, but the peaks split into two at around 31° for γ-Li_3PS_4, which is a unique peak not observed for β-Li_3PS_4. The samples with x = 0.0250 and 0.0375 showed weak peaks corresponding to γ-Li_3PS_4, indicating that γ-Li_3PS_4 and β-Li_3PS_4 are in a mixed phase. Quantification of γ-Li_3PS_4 and β-Li_3PS_4 will be discussed in ³¹P NMR experiments.

It has been reported that the phase transition of γ-Li_3PS_4 to β-Li_3PS_4 for Li_3PS_4 without Ca doping occurs above 573 K.[23] Unassigned peaks marked with filled orange circles (Unknown1) were observed for $Li_{3-2x}Ca_xPS_4$ at 2θ = 20.3, 21.5, 28.1, 28.5, and 32.2°. It is noted that the peak patterns for CaS[42] and Ca phosphorus sulfides ($Ca_2P_2S_6$)[43] cannot be assigned to Unknown1 as unreacted raw compounds. The relative intensities of the peaks from Unknown1 increased with an increase in Ca doping. The peaks at around 56.8° on the high-angle side were shifted to the lower-angle side when x was changed from 0 to 0.05, as shown in Figure 1 (right-hand panel). This behavior is associated with lattice expansion caused by increasing the amount of Ca doping. A slight low-angle shift was observed when x changed from 0.1 to 0.15. This may be due to the fact that excess Ca doping causes the shrunken lattice with increasing Coulombic interaction between Ca^{2+} and PS_4^{3-} involving increasing vacancies. Two peak intensities at around 18° varied with the amount of doping. This corresponds to a change in the elemental composition caused by Ca doping. The main peak at around 18° in the doped sample was assigned to the β-Li_3PS_4 phase, as indicated by the ³¹P NMR result discussed later.

The lattice constants and volumes for $Li_{3-2x}Ca_xPS_4$ derived from the Rietveld refinement of experimental XRD patterns considering the β-Li_3PS_4 phase are shown in Figure 2 as
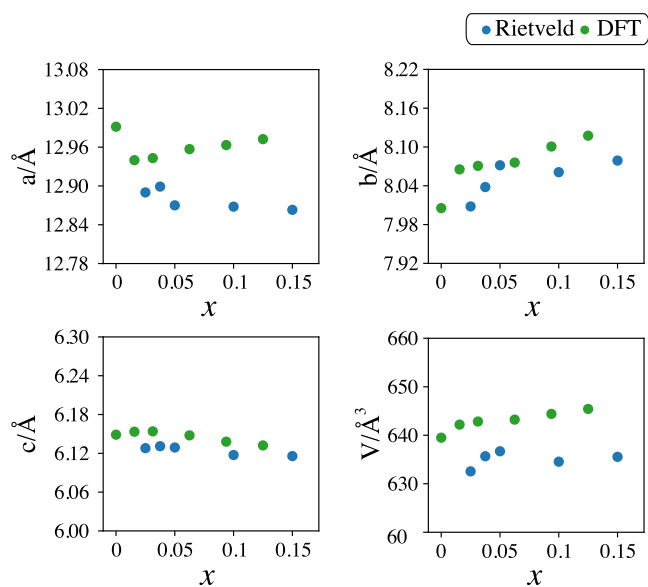
Figure 2. Lattice constants and unit-cell volume changes of $Li_{3-2x}Ca_xPS_4$. The filled blue and green circles show the values evaluated from Rietveld refinement and DFT calculations of β-Li_3PS_4, respectively.

functions of x. The fitting results of Rietveld refinement with experimental data, R-factors, and χ^2 (goodness of fit) values for $Li_{3-2x}Ca_xPS_4$ are shown in Figure S1 of Supporting Information. The lattice volume of the β phase increased with increasing Ca doping up to $x = 0.0500$, as expected from the change in the peak positions at around 56.8°. In particular, the increase in the lattice constant b was significant compared to the changes in a and c. This change in the lattice constant corresponds to substitution of smaller Li^+ (ionic radius 0.68 Å) with Ca^{2+} (0.99 Å); thus, Ca^{2+} doping can be successfully achieved by the solid-phase reaction. There may be a slight possibility of the substitution of P^{5+} and Ca^{2+}. This substitution changes PS_4^{3-}, and it disrupts the crystal structure. The appearance of major β-Li_3PS_4 crystalline peaks proves that the substitution of P^{5+} for Ca^{2+} did not occur.

The XRD patterns of $Li_{2.9}Ca_yBa_{0.05-y}PS_4$ ($y = 0$, 0.005, 0.015, 0.025, 0.035, and 0.045) are shown in Figure 3. Unassigned peaks marked with purple rhombuses (Unknown2) at $2\theta = 10.5$, 14.7, 20.9, 23.4, 31.7, 34.4, and 35.1° were also observed for all $Li_{2.9}Ca_yBa_{0.05-y}PS_4$ samples. Note that these peaks do not match those predicted for BaS[44] or $Ba_2P_2S_6$.[45] The samples with $y = 0$ and 0.005 exhibit multiple splitting of diffraction peaks at around 31°, suggesting the existence of mixed γ-Li_3PS_4 and β-Li_3PS_4 phases.

A peak shift at around 56.8° toward the higher-angle side was found for samples with increasing y, as shown in Figure 3 (right-hand panel). This peak shift occurred continuously as y increased. This continuous shift was related to the lattice shrinkage with doping by Ca instead of Ba in β-Li_3PS_4. This result is simply explained by the ionic radius; the larger ionic radius of Ba^{2+} compared to that of Ca^{2+} contributes to the increased lattice expansion. Sulfide materials composed of P and S have anions in a variety of PS units. β-Li_3PS_4 and γ-Li_3PS_4 phases are composed of PS_4^{3-} alone, but unknown peaks may originate from the conversion of PS_4^{3-} to $P_2S_6^{4-}$ or $P_2S_7^{4-}$. Since such conversions of PS units are difficult to identify by diffraction patterns, the local structure of P was analyzed using ^{31}P NMR.

The filled blue circles in Figure 4 show the lattice constants and volume changes for $Li_{2.9}Ca_yBa_{0.05-y}PS_4$ determined from the Rietveld refinement of the experimental data. As predicted by the observed peak at around 56.8°, the volume of codoped $Li_{2.9}Ca_yBa_{0.05-y}PS_4$ decreased with increasing Ca doping.

4.2. AC Impedance Measurements. Nyquist plots obtained from impedance measurements and the conductivity for all samples with variable temperature are listed in Figure S2 and Table S1.

Figure 5a shows the logarithmic ionic conductivities, σ, of $Li_{3-2x}Ca_xPS_4$ ($x = 0$, 0.0250, 0.0375, 0.0500, 0.1000, and 0.1500) as functions of inverse temperature. The solid lines indicate the linear regression results to evaluate the activation energy E_a based on the Arrhenius law

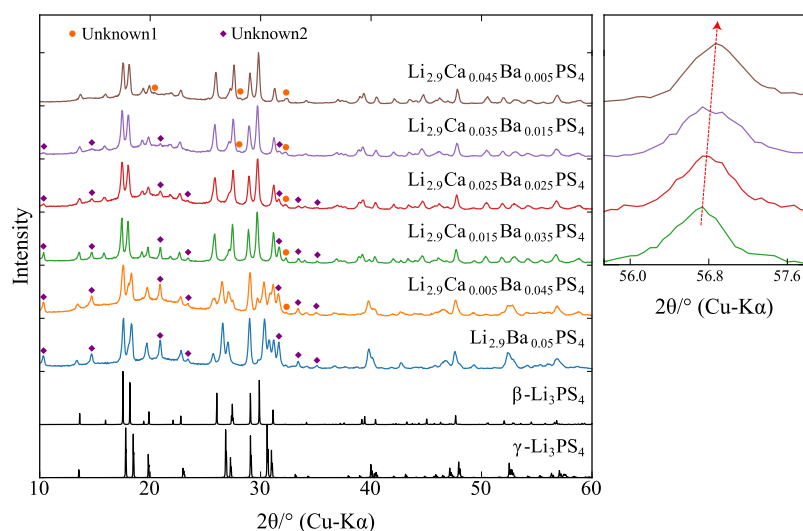$$\sigma T \propto \exp\left(-\frac{E_a}{RT}\right) \tag{1}$$

Figure 3. XRD patterns for $Li_{2.9}Ca_yBa_{0.05-y}PS_4$ ($y = 0$, 0.005, 0.015, 0.025, 0.035, and 0.045) and referenced crystalline data for γ-Li_3PS_4 and β-Li_3PS_4. Selected peaks are shown enlarged in the right-hand panel to highlight the peak shift with compositional change.
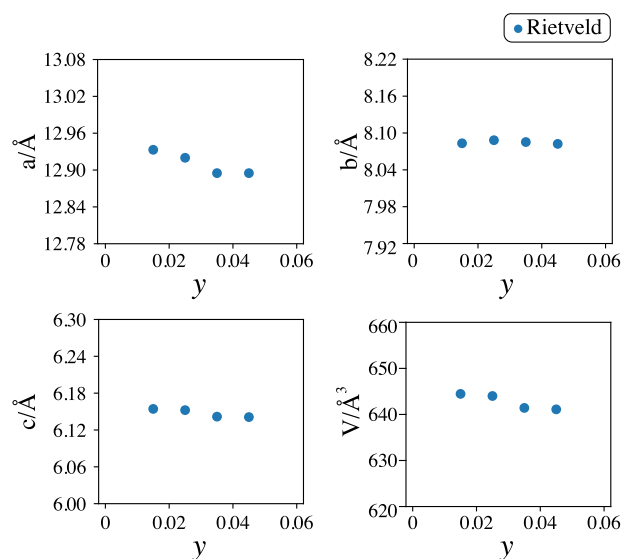
Figure 4. Lattice constants and unit-cell volumes of $Li_{2.9}Ca_yBa_{0.05-y}PS_4$ as functions of y, as derived from Rietveld refinement of β-Li_3PS_4.

where σ, T, and R are the conductivity, temperature, and gas constant, respectively. The values of E_a were calculated from the slopes of the lines in Figure 5a. The values of σ at 300 K, σ_{RT}, and the derived activation energies are also displayed as functions of x in $Li_{3-2x}Ca_xPS_4$ (Figure 5b). All values of σ_{RT} and E_a are listed in Table S2 of the Supporting Information. The σ_{RT} value of γ-Li_3PS_4 without Ca doping was 4.84×10^{-7} S cm^{-1}, which is in good agreement with a previous result for γ-Li_3PS_4 synthesized by solid-state reaction.[22]

The σ_{RT} values were dramatically enhanced by 2 orders of magnitude with Ca doping. This behavior is attributed to the formation of the β-Li_3PS_4 phase, which has a higher conductivity than the γ-Li_3PS_4 phase at room temperature. The maximum σ_{RT} value was found for the sample with $x = 0.0500$; samples with doping above $x = 0.0500$ have lower σ_{RT} values. The E_a values of γ-Li_3PS_4 and β-Li_3PS_4 were slightly higher than those previously reported.[23,24,40] This difference may be due to the synthesis conditions and the effects of the formation of unknown phases. The E_a value increased with increasing Ca doping, as shown in Figure 5b. The trends of σ_{RT} and E_a with x are explained by the formation of the unknown phases observed in Figure 1 and the effect of excess Ca doping. An increase of E_a with increasing Ca doping has also been found for solid-state Na$^+$ electrolytes, denoted as $Na_{3-2x}Ca_xPS_4$.[31] Although a variety of factors contribute to the conductivity of samples that are not single-phase, the vacancies likely created by Ca doping in monovalent solid-state electrolytes generate a conduction path with an increased activation barrier for monovalent cations.

Figure 6a,b shows Arrhenius plots of σ as functions of inverse temperature, and σ_{RT} and E_a as functions of y in $Li_{2.9}Ca_yBa_{0.05-y}PS_4$. These values are summarized in Table S3. Intermediate σ_{RT} values were found for γ-Li_3PS_4 and β-Li_3PS_4 samples with $y = 0$ and 0.005. This result is expected from the mixing of the γ-Li_3PS_4 and β-Li_3PS_4 phases. In fact, a characteristic peak at around 31° attributed to the γ-Li_3PS_4 phase can be observed in the XRD pattern in Figure 3. A convex change of σ_{RT} against y is found in Figure 6b, and the maximum σ_{RT} value was obtained for the sample with $y = 0.025$.

The σ_{RT} values of $Li_{2.9}Ca_yBa_{0.05-y}PS_4$ were about 1.5−2.0 times larger than those of $Li_{3-2x}Ca_xPS_4$. The lattice expansion
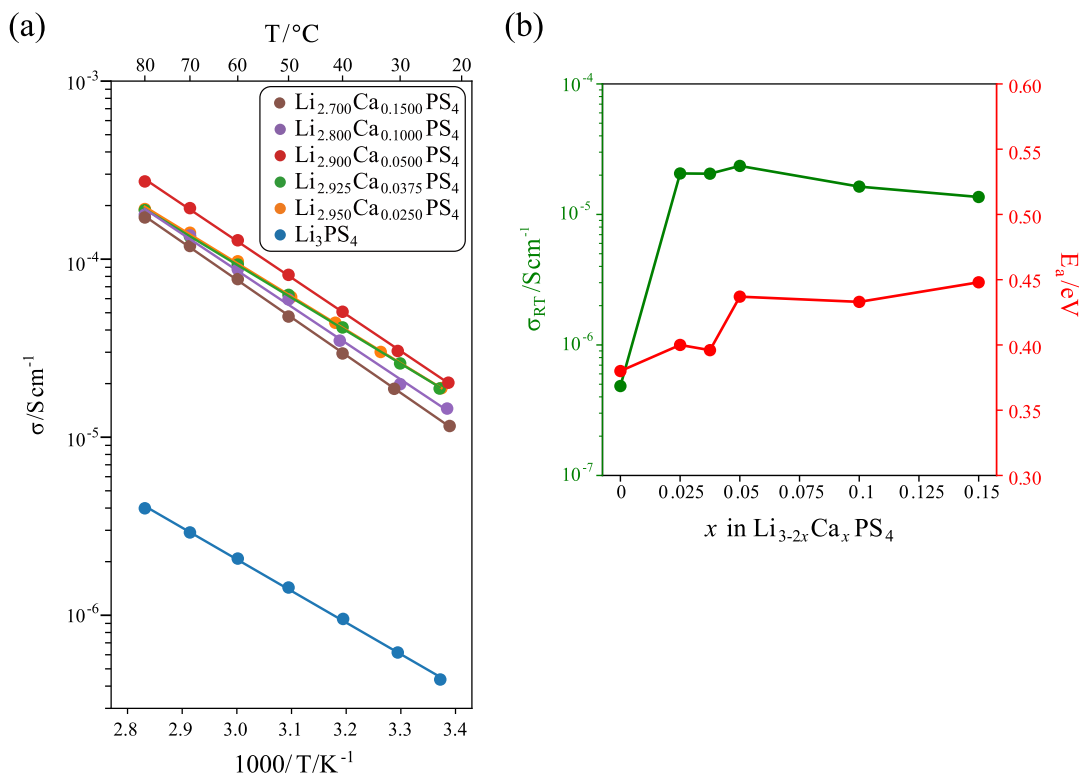
Figure 5. (a) Arrhenius plots of ionic conductivities of $Li_{3-2x}Ca_xPS_4$. (b) σ_{RT} and E_a as functions of x in $Li_{3-2x}Ca_xPS_4$.
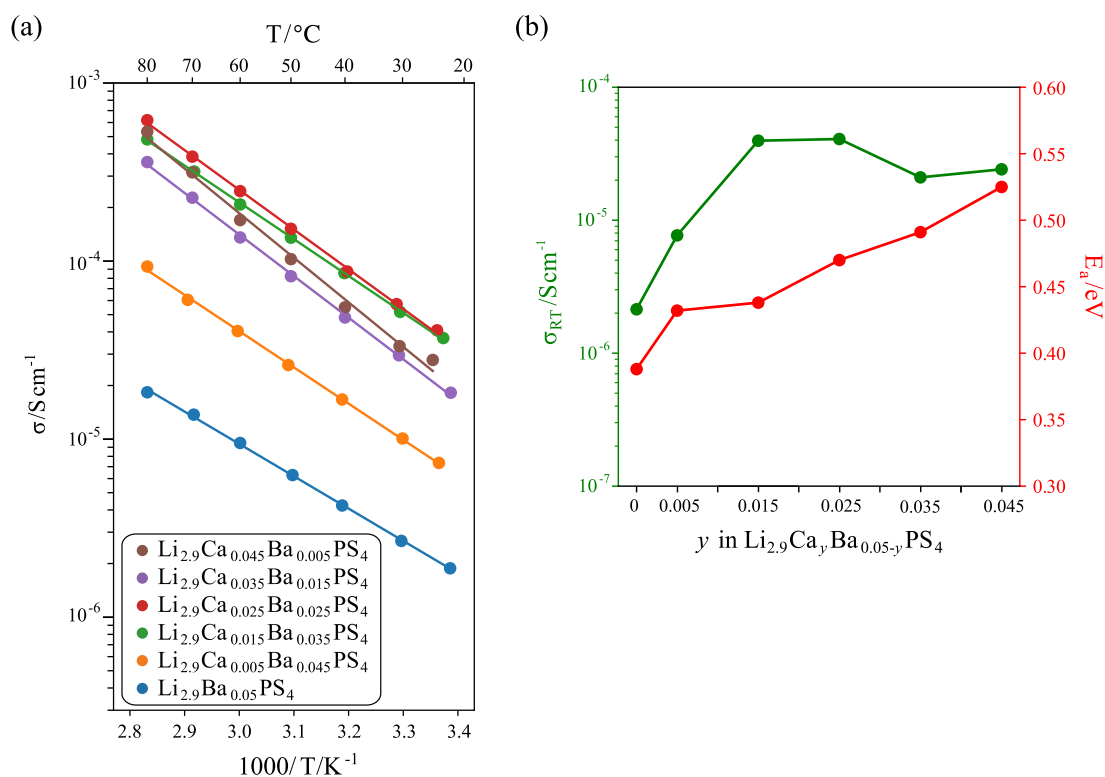
Figure 6. (a) Arrhenius plots of the σ value of $Li_{2.9}Ca_yBa_{0.05-y}PS_4$ as functions of inverse temperature. (b) Plots of σ_{RT} and E_a conductivity versus y.
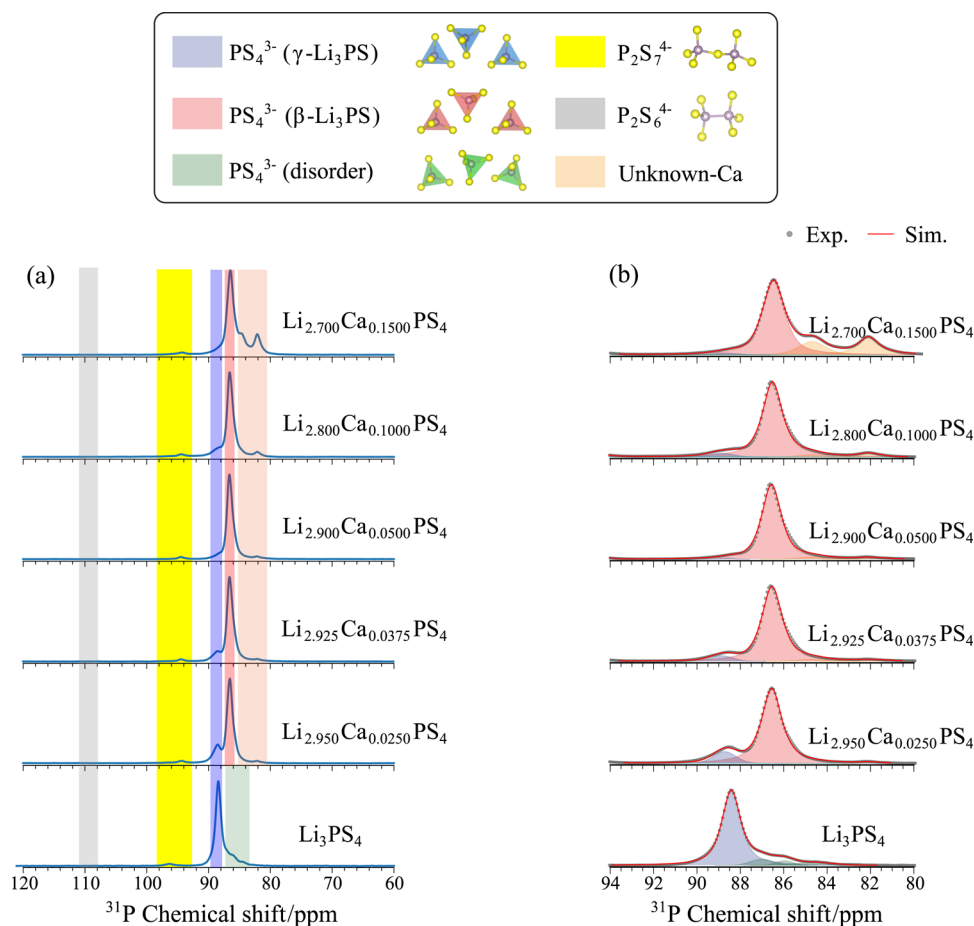

Figure 7. (a) ^{31}P MASNMR spectra and (b) deconvolved ^{31}P MASNMR spectra of $Li_{3-2x}Ca_xPS_4$ (x = 0, 0.0250, 0.0375, 0.0500, 0.1000, and 0.1500).

induced by Ba doping generated an efficient conduction path for Li$^+$. However, the E_a value of Li$_{2.9}$Ca$_y$Ba$_{0.05-y}$PS$_4$ tends to be larger than that of Li$_{3-2x}$Ca$_x$PS$_4$. The enlargement of the Li$^+$ conduction path resulting from the lattice expansion generates new Li$^+$ conduction paths; however, this does not contribute to the reduction of the migration barrier.

4.3. ^{31}P Solid-State NMR. ^{31}P MAS NMR measurements were performed to evaluate the local ^{31}P structure and quantify the PS units in the sample. Figure 7 shows the ^{31}P MAS spectra of Li$_{3-2x}$Ca$_x$PS$_4$ along with peak assignments expected from previous ^{31}P NMR studies of phosphate sulfide.[40,46−49] There are no peaks originating from phosphate units in the lower-frequency side ranging from 50 to −100 ppm,[50,51] indicating that there is no contamination of oxygen during synthesis. The peak assignments are indicated by filled rectangles of different colors, with spans showing their chemical shift ranges. The experimental ^{31}P MAS NMR spectra were deconvolved based on six peaks corresponding to possible PS units. The main peaks observed ranged from 94 to 80 ppm, and these are magnified and displayed with the deconvolved results in Figure 7 (right-hand panel).

Although the crystalline structures of γ-Li$_3$PS$_4$ and β-Li$_3$PS$_4$ are composed of only PS$_4^{3-}$, the ^{31}P chemical shift of PS$_4^{3-}$ for γ-Li$_3$PS$_4$ differs from that of β-Li$_3$PS$_4$.[47] The ^{31}P chemical shift of disordered PS$_4^{3-}$ units was also different from those of γ-Li$_3$PS$_4$ and β-Li$_3$PS$_4$. The ^{31}P chemical shift ranges of PS$_4^{3-}$ in γ-Li$_3$PS$_4$, β-Li$_3$PS$_4$, and disordered units were 89 ± 2, 86 ± 2, and 85 ± 2 ppm, respectively.[40,46,47,52] These known chemical shift ranges were imposed as the constraints for the spectral deconvolution, and they produced reasonable simulated spectra, as shown in Figure 7 (right-hand panel). The population of two PS$_4^{3-}$ in β-Li$_3$PS$_4$ and γ-Li$_3$PS$_4$ and disordered PS$_4^{3-}$ was obtained from the peak areas in the deconvolved spectra. Note that such quantitative information for the cophases cannot be accessed from the XRD patterns alone. The mixed phases with γ-Li$_3$PS$_4$ and β-Li$_3$PS$_4$ were expected from the diffraction patterns of the sample with lower Ca doping, which was consistent with results quantified in the ^{31}P MAS NMR spectrum. Unknown peaks in the ^{31}P MAS NMR spectrum of Li$_{3-2x}$Ca$_x$PS$_4$ with $x = 0.1500$ were observed on the higher-magnetic-field side, ranging from 86 to 80 ppm. The ^{31}P chemical shift can be assigned to PS units near Ca^{2+}. This trend has also been reported for phosphate glasses containing alkaline-earth cations.[53−55] This local structure is related to the crystalline compounds observed in the XRD patterns of Figure 1.

Disordered PS$_4^{3-}$ was present in crystalline γ-Li$_3$PS$_4$ with $x = 0$, as shown in the peak filled with green at around 85 ppm. A small amount of P$_2$S$_7^{4-}$ and a negligible amount of P$_2$S$_6^{4-}$ in Li$_{3-2x}$Ca$_x$PS$_4$ were observed at around 96 and 110 ppm, as shown by the yellow and gray areas. Additional peaks colored pale pink on the higher-field side ranging from 80 to 86 ppm for Li$_{2.9}$Ca$_y$Ba$_{0.05-y}$PS$_4$ were confirmed for all samples except for $x = 0$. Although these peaks are hard to distinguish from disordered PS$_4^{3-}$ due to line broadening, these were assigned to PS units in unknown phases based on the XRD results in Figure 1.

The populations as functions of x in Li$_{3-2x}$Ca$_x$PS$_4$ are displayed in Figure 8 along with the σ_{RT} results. All populations of the PS units and the chemical shifts derived from the spectral deconvolution are summarized in Table S4 of the Supporting Information The introduction of a small amount of Ca doping ($x = 0.0250$) clearly increased the amount of PS$_4^{3-}$
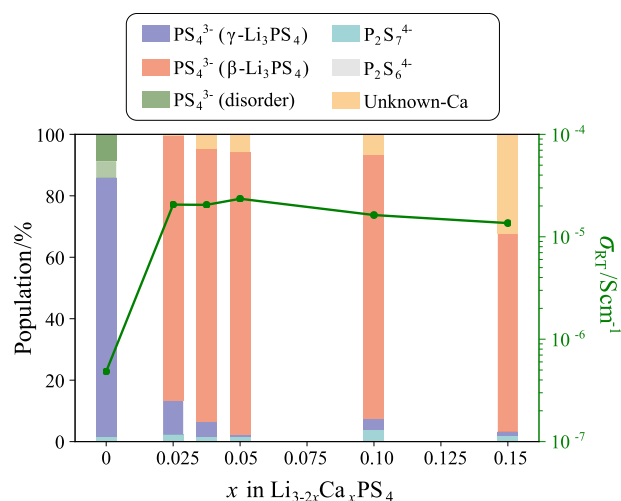

Figure 8. Populations of PS units and unknown phases and conductivities at room temperature in Li$_{3-2x}$Ca$_x$PS$_4$ ($x = 0$, 0.2500, 0.0375, 0.0500, 0.1000, and 0.1500) as functions of x.

in the β-Li$_3$PS$_4$ phase, which is consistent with the XRD results in Figure 1. The maximum β-Li$_3$PS$_4$ content was found at $x = 0.0500$, which is consistent with a composition exhibiting the maximum σ_{RT}. Excess Ca doping above $x = 0.1000$ induces the formation of PS units in unknown phases and consequently leads to a decrease in σ_{RT}.

Figure 9 shows the experimental and deconvolved ^{31}P MAS NMR spectra of Li$_{2.9}$Ca$_y$Ba$_{0.05-y}$PS$_4$ from the same procedure as that used to obtain the spectra of Li$_{3-2x}$Ca$_x$PS$_4$. The peak assignments are displayed by using different colors, as in Figure 7. The PS$_4^{3-}$ in both the β-Li$_3$PS$_4$ and γ-Li$_3$PS$_4$ phases are present in the samples doped only with Ba ($y = 0$). When Ca was additionally introduced into the sample, the PS$_4^{3-}$ of γ-Li$_3$PS$_4$ was not visible. These changes were consistent with the XRD results in Figure 3.

Unknown peaks (unknown-Ca and unknown-Ba) in the ^{31}P MAS NMR spectra of Li$_{2.9}$Ca$_y$Ba$_{0.05-y}$PS$_4$ with $y = 0$ were observed at around 64, 67, and 79 ppm. These peaks may be assigned to PS units related to the Ba^{2+} and Ca^{2+} positions. The populations of these unknown peaks slightly decreased with increasing Ca doping. The peak assigned to PS$_4^{3-}$ of γ-Li$_3$PS$_4$ was almost invisible for samples above $y = 0.025$.

Figure 10 shows the relationships between the PS-unit populations derived from the deconvolution of the ^{31}P MAS NMR spectra and the σ_{RT} value of Li$_{2.9}$Ca$_y$Ba$_{0.05-y}$PS$_4$ as a function of y. Table S5 summarizes the chemical shifts of ^{31}P and the populations of PS units, including unknown crystalline phases for Li$_{2.9}$Ca$_y$Ba$_{0.05-y}$PS$_4$. The population of β-Li$_3$PS$_4$ reached about 95% for the sample with $y = 0.150$. Consistency of σ_{RT} changes with the amount of the β-Li$_3$PS$_4$ phase was also found with Li$_{3-2x}$Ca$_x$PS$_4$.

4.4. ^{7}Li MAS NMR. Identification of Li species based on mobility was investigated using ^{7}Li MAS NMR. The line widths of the peaks on the ^{7}Li MAS spectra are related to the rotational correlation time (spin−spin relaxation time), meaning that mobile and immobile Li$^+$ can be differentiated by narrow and broadened peaks.[56,57] Figure 11 shows the ^{7}Li MAS NMR spectra of selected Li$_{3-2x}$Ca$_x$PS$_4$ and Li$_{2.9}$Ca$_y$Ba$_{0.05-y}$PS$_4$ samples along with deconvolved results, showing three peaks. The number of peaks could not be determined definitively; however, deconvolution with two
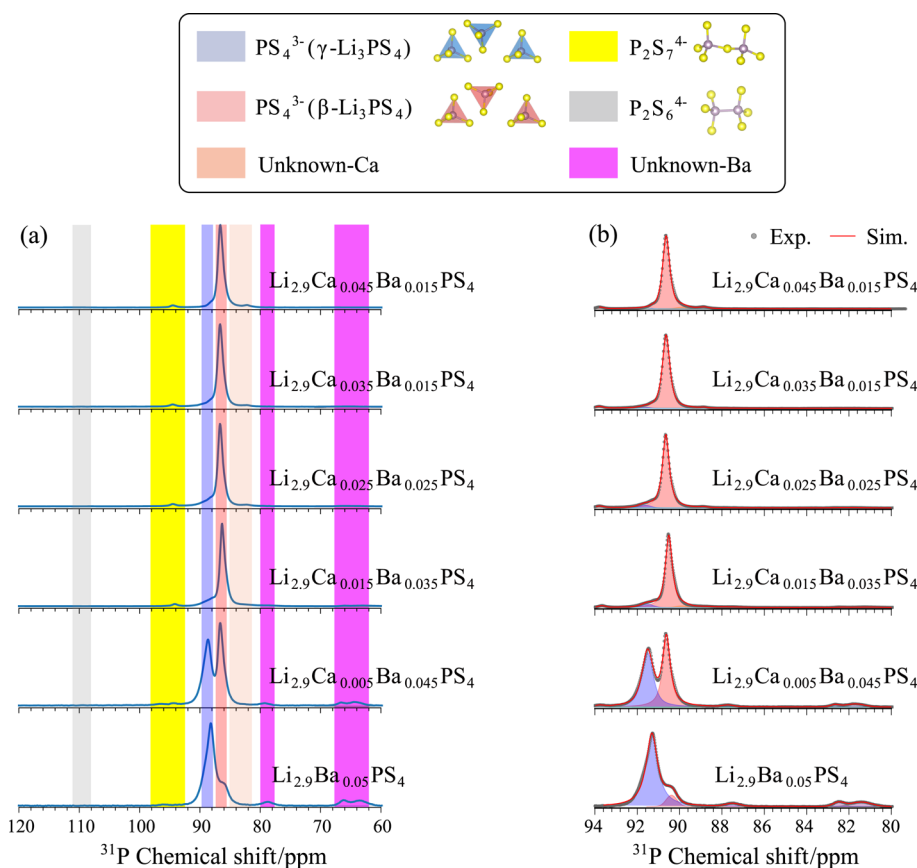
Figure 9. (a) ^{31}P MAS NMR spectra of $Li_{2.9}Ca_yBa_{0.05-y}PS_4$ with the assignments of PS units displayed using different colors. (b) Deconvolved results of experimental and simulated ^{31}P MAS NMR spectra for the main peak region.
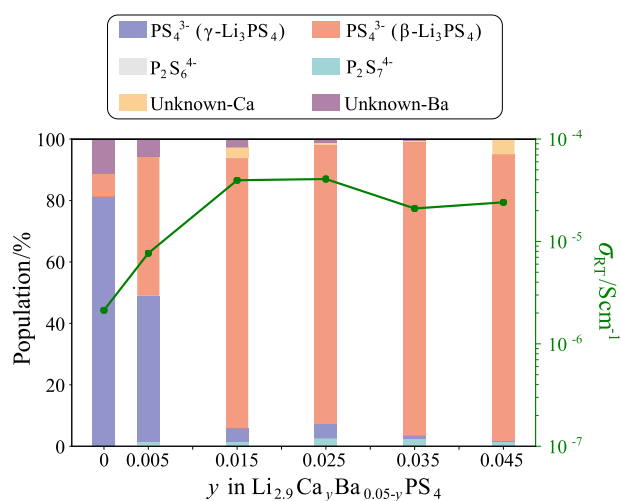

Figure 10. Populations of PS units and unknown phases and conductivities at room temperature of $Li_{2.9}Ca_yBa_{0.05-y}PS_4$ ($y = 0$, 0.005, 0.015, 0.025, 0.035, and 0.045) as functions of y.

immobile and one mobile Li^+ species represents the experimental spectra well. The chemical shifts and populations derived from the deconvolution are summarized in Table S6 of the Supporting Information.

A single broadened peak at around 1.5 ppm was observed for γ-Li_3PS_4 without doping, which corresponds to immobile Li^+ species. The ^7Li chemical shift of the immobile Li^+ is close to the results of previous ^7Li NMR studies of γ-Li_3PS_4.[46] However, mobile Li^+, with a narrow peak at around 1 ppm,

appeared for $Li_{3-2x}Ca_xPS_4$ and $Li_{2.9}Ca_yBa_{0.05-y}PS_4$ instead of decreasing in immobile Li^+. The appearance of these mobile Li^+ when doping with Ca and Ba is consistent with increasing σ_{RT}.

The fast exchange of Li^+ between 8d and 4b sites at the NMR time scale has been reported.[56,57] This fast exchange is associated with the narrow peak and conduction path along the b axis in β-Li_3PS_4[40] revealed by bond-valence-sum analysis for X-ray and neutron diffraction data. The mobile Li^+ can likely be assigned to exchange of Li^+ between 8d and 4b within the NMR time scale.

The population of the broadened peak (immobile) in $Li_{3-2x}Ca_xPS_4$ with $x = 0.1500$ was relatively higher than that found in $Li_{3-2x}Ca_xPS_4$ with $x = 0.0500$. Since $Li_{3-2x}Ca_xPS_4$ with $x = 0.1500$ contains a more unknown crystalline phase than that with $x = 0.0500$, the immobile2 peak was assigned to Li^+ in another unknown crystalline phase. The Li^+ mobility in the unknown crystalline phase is not as high as expected from the results of the conductivity measurement.

The populations of Li^+ species and σ_{RT} in selected γ-Li_3PS_4, $Li_{3-2x}Ca_xPS_4$, and $Li_{2.9}Ca_yBa_{0.05-y}PS_4$ samples are displayed in Figure 12 along with their σ_{RT} values. The populations of mobile Li^+ were well-correlated with the σ_{RT} values for all samples. It is clear that the large amount of highly mobile Li^+ detected by ^7Li MAS NMR is key to achieving a superior Li^+ conductivity. The amount of mobile Li does not reach 50%, even in the best Li^+-conductive sample ($Li_{2.9}Ca_{0.025}Ba_{0.025}PS_4$). This result suggests the possibility of improving the Li^+ conductivity by further modifying the β-Li_3PS_4 structure.
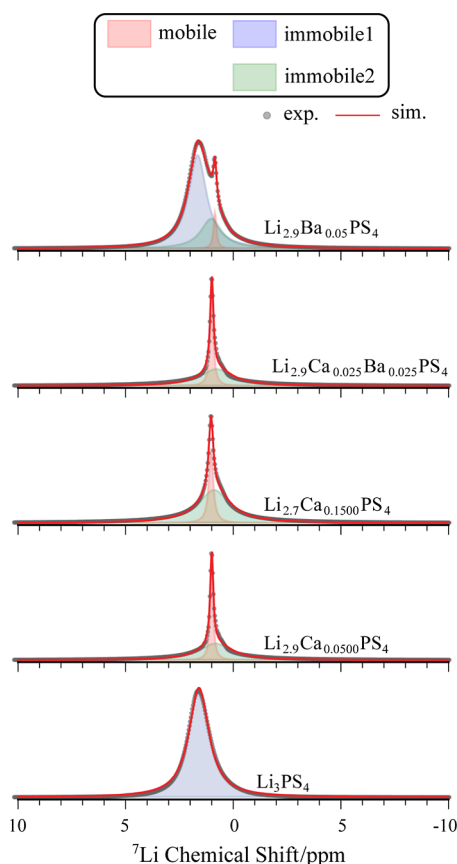
Figure 11. Deconvolved ^{7}Li MAS NMR spectra of Li$_{3-2x}$Ca$_x$PS$_4$ (x = 0, 0.0500, and 0.1500) and Li$_{2.9}$Ca$_y$Ba$_{0.05-y}$PS$_4$ (y = 0.025 and 0.050). The reference sample was a 1 M LiCl solution.
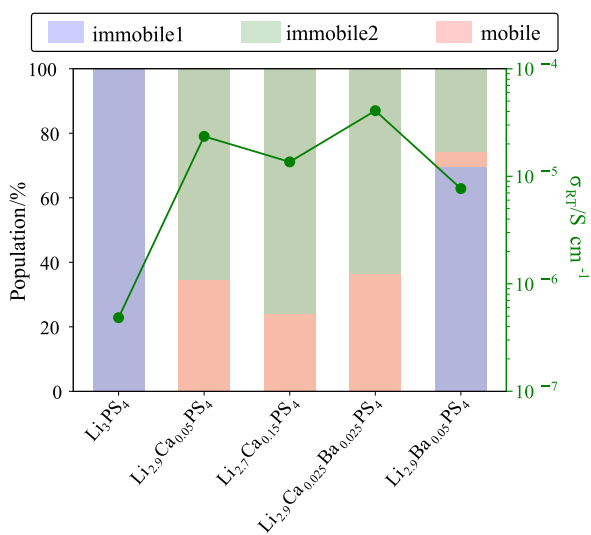

Figure 12. Populations of one mobile and two immobile Li$^+$ species evaluated from ^{7}Li MAS NMR spectra of selected Li$_{3-2x}$Ca$_x$PS$_4$ and Li$_{2.9}$Ca$_y$Ba$_{0.05-y}$PS$_4$ samples. The σ_{RT} value for each sample is displayed as a reference.

4.5. DFT Calculations.

The stability of β-Li$_3$PS$_4$ resulting from doping with Ca was theoretically investigated by using DFT calculations. The initial structures were made from crystalline β-Li$_3$PS$_4$ and γ-Li$_3$PS$_4$ with various x values in Li$_{3-2x}$Ca$_x$PS$_4$. The values of x were chosen to match the synthesized samples as closely as possible. To compare the

system energies of the β-Li$_3$PS$_4$ and γ-Li$_3$PS$_4$ structures, we gave them both the same atomic composition. The compositions for DFT calculations were x = 0, 0.0156, 0.0312, 0.0625, 0.0938, and 0.1250, corresponding to 1, 2, 4, 6, and 8 substitutions of Li with Ca.

The stability of the β-Li$_3$PS$_4$ and γ-Li$_3$PS$_4$ structures was estimated by the difference in the enthalpy, H, obtained from the DFT calculations. The H values were evaluated for each system after structural optimization of the atomic positions and lattice constants.

The obtained lattice constants of Li$_{3-2x}$Ca$_x$PS$_4$ with β-Li$_3$PS$_4$ from the DFT calculations are displayed in Figure 2 along with the experimental results from Rietveld analysis. All lattice constants and volumes are also summarized in Table S7 of the Supporting Information. The lattice constants of Li$_{3-2x}$Ca$_x$PS$_4$ for the β-Li$_3$PS$_4$ lattice obtained from DFT were somewhat larger overall than those obtained from the experiments. This trend can be reasonably explained by overestimation of the bond lengths for the DFT calculations by the GGA-PBE exchange−correlation approximation;[58,59] this overestimation of the bond lengths leads to a larger lattice. Although such errors are included in the DFT results, the trend in the lattice constant with different x values in Li$_{3-2x}$Ca$_x$PS$_4$ matches well with the experimental results. For instance, the lattice parameters b and c showed an increasing trend with increasing x. Therefore, the H values obtained from the structural optimization are considered to be a good representation of real samples.

The H values of β-Li$_3$PS$_4$ and γ-Li$_3$PS$_4$ structures with the same composition are indicated in Figure 13 as functions of x
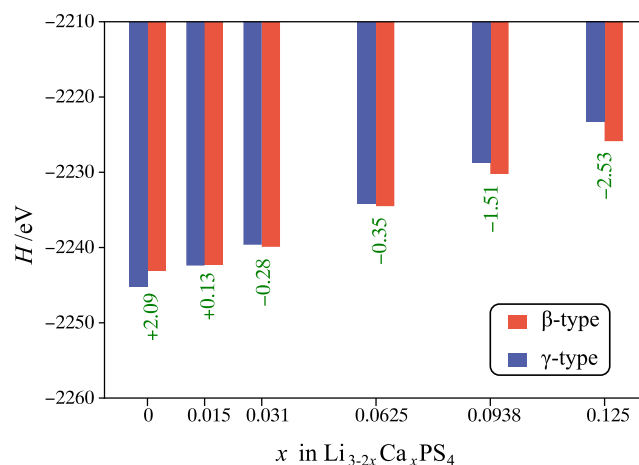
Figure 13. Enthalpy H of Li$_{3-2x}$Ca$_x$PS$_4$ (x = 0, 0.0156, 0.0312, 0.0625, 0.0938, and 0.1250) for the β-Li$_3$PS$_4$ and γ-Li$_3$PS$_4$ lattices. The differences between the enthalpy ΔH are indicated in green text.

in Li$_{3-2x}$Ca$_x$PS$_4$. The differences in H (ΔH) for β-Li$_3$PS$_4$ and γ-Li$_3$PS$_4$ are displayed at the bottom of each bar in Figure 13. The ΔH value of Li$_3$PS$_4$ without Ca doping was 2.09 eV, meaning that γ-Li$_3$PS$_4$ is more stable than β-Li$_3$PS$_4$. It should be noted that the DFT calculations do not take into account thermal effects (under vacuum at 0 K). However, the lower H value of γ-Li$_3$PS$_4$ when compared to that of β-Li$_3$PS$_4$ rationalizes the preferential formation of γ-Li$_3$PS$_4$ at room temperature via the solid-state reaction route. For the composition with only a small amount of Ca doping (x = 0.0156), γ-Li$_3$PS$_4$ is still somewhat more stable. In systems with Ca doping above x = 0.0312, the stable phase transfers to

the β-Li$_3$PS$_4$ lattice. This perspective on ΔH is consistent with the experimental formation of the β phase by doping with Ca.

5. DISCUSSION

Although a complete single phase could not be obtained via the solid-state reaction, β-Li$_3$PS$_4$, as the high-temperature phase, is stabilized by Ca or Ba doping at room temperature. The changes in the σ_{RT} values of the synthesized samples were consistent with the amount of the β-Li$_3$PS$_4$ phase, which was quantitatively evaluated by ^{31}P MAS NMR. The ideal Li$^+$ conductivity of the single-phase β-Li$_3$PS$_4$ at room temperature was derived from the extrapolation of data ranging from 473 to 573 K.[22,24] The extrapolated value at room temperature is 8.9 $\times$ 10^{-7} S cm^{-1}, which is approximately 2 orders of magnitude lower than that of the divalent doped β-Li$_3$PS$_4$ in this study. This gap suggests that Li$^+$ conduction in divalent doped β-Li$_3$PS$_4$ is elevated by developing a path not present in the pure β-Li$_3$PS$_4$ phase. The volume expansion along the b axis is also related to the development of this conduction path and the change of the Li$^+$ migration barrier.

The activation energy of the β-Li$_3$PS$_4$ phase with divalent doping was higher than that of β-Li$_3$PS$_4$ without doping. Therefore, the new conduction mechanism, which involves the generation of new conduction paths in divalent cation doping of β-Li$_3$PS$_4$, contributes to an increase in Li$^+$ conductivity rather than a reduction in the Li$^+$ migration barrier.

It is expected that the formation of Li$^+$ vacancies caused by divalent doping in β-Li$_3$PS$_4$ reduces the frequency of ballistic Li$-$Li interactions. The "billiard-ball" mechanism of enhancing Li$^+$ conduction has been proposed in recent experimental and theoretical studies of argyrodite-type lithium conductors.[60] In this process, the kinetic energy required for Li$^+$ migration can be relayed from one ion to another via cascade processes. The contribution of this effect is likely enhanced by the presence of vacancies. In a perfect β-Li$_3$PS$_4$ crystal without defects, the kinetic energy of Li$^+$ migration is consumed by stationary vibrational motion, which cannot contribute to long-distance Li$^+$ translational motion.

Ca and Ba codoping in β-Li$_3$PS$_4$ can expand the conduction path from that of β-Li$_3$PS$_4$, and this can be simply explained by the Ba^{2+} ions being larger than the Ca^{2+} ions. The Li$^+$ conductivity of β-Li$_3$PS$_4$ with Ca and Ba doping (Li$_{2.9}$Ca$_{0.025}$Ba$_{0.035}$PS$_4$) is about twice that of the sample with only Ca doping (Li$_{2.9}$Ca$_{0.05}$PS$_4$), as indicated in Tables S2 and S3, when comparing samples with the same amount of divalent doping. This result suggests that an appropriate extension of the conductive path can be controlled by codoping, and this can enhance the Li$^+$ conductivity.

It has been reported that the formation of Li$^+$ vacancies is needed to stabilize the high-temperature phase of oxide Li$_7$La$_3$Zr$_2$O$_{12}$.[61,62] The application of the same idea to the sulfide has now also been demonstrated; thus, the stability of β-Li$_3$PS$_4$ involving vacancies has been theoretically revealed by DFT calculations. This phenomenon was associated with an increasing entropy by introducing divalent cations and involving vacancies. The structural disorder present in Ca-doped β-Li$_3$PS$_4$ was visually identified, as shown in the atomic images of Figure S3 of Supporting Information. The degree of disorder for β-Li$_3$PS$_4$ with Ca doping is higher than that for γ-Li$_3$PS$_4$.

Such disordering of Li$^+$ sites is associated with a variety of conduction routes, which can promote Li$^+$ conduction by means of the billiard-ball mechanism. These cascade processes can be facilitated by diverse Li$^+$ sites in the conduction paths. The introduction of defects and path extension cause the generation of a variety of Li$^+$ sites corresponding to an increase in entropy, which can work in conjunction with the enhancement of the billiard-ball mechanism. Changes in the Li$^+$ dynamics with doping are necessary to understand the macroscopic conductivity. The details of the dynamic behavior of Li$^+$ will be revealed by molecular dynamics simulation based on the structures modeled in this study.

6. CONCLUSIONS

The high-temperature β-Li$_3$PS$_4$ phase was successfully stabilized at room temperature by divalent cation doping by using a solid-phase reaction route. The generation of the β-Li$_3$PS$_4$ phase was examined by XRD and subsequent Rietveld analysis. The expansion of the lattice with divalent cation doping was demonstrated using ^{31}P MAS NMR. The maximum Li$^+$ conductivity obtained by divalent doping was more than 2 orders of magnitude higher than that of γ-Li$_3$PS$_4$ with the low-temperature phase. The Li$^+$ conductivity is dependent on the amount of the β-Li$_3$PS$_4$ phase. Unknown phases with lower Li$^+$ conductivity were induced with excess Ca doping, and these were tentatively assigned to PS units positioned near Ca^{2+}.

The population of mobile Li$^+$ was revealed by ^{7}Li MAS NMR spectra. The increase in Li$^+$ conductivity was consistent with the increased amount of mobile Li. The population of mobile Li$^+$ was about 25%, meaning that a proportion of Li$^+$ cannot work as conduction carriers. Converting such immobile Li$^+$ to mobile Li$^+$ is likely to enhance the Li$^+$ conductivity further.

Crystalline structures of composition equivalent to that of the synthesized samples with Ca doping for the γ-Li$_3$PS$_4$ and β-Li$_3$PS$_4$ lattices were reproduced using DFT calculations. The stability of the β-Li$_3$PS$_4$ phase with suitable Ca doping at room temperature was theoretically demonstrated by considering the enthalpy. Defects produced by the substitution of Li$^+$ with divalent cations induce disordering involving a variety of Li$^+$ sites. The degree of disordering in β-Li$_3$PS$_4$ is significant compared to that in γ-Li$_3$PS$_4$. This result can be attributed to a variety of different Li$^+$ conduction paths compared to that formed by ordered Li$^+$ sites. It is expected that the modification of Li$^+$ conduction paths induced by doping with divalent cations can enhance a billiard-ball mechanism involving cascade processes to improve long-range Li migration. As a result, the experimentally observed macroscopic conductivity is higher.

The introduction of defects by doping with divalent cations and controlling the conduction paths represent important concepts for the modification and optimization of existing crystals. Improving the performance of materials based on these concepts can contribute to the realization of solid-state batteries.

■ ASSOCIATED CONTENT

ⓈI Supporting Information

The Supporting Information is available free of charge at https://pubs.acs.org/doi/10.1021/acsomega.3c09952.

Rietveld refinement of XRD patterns for Li$_{3-2x}$Ca$_x$PS$_4$ and Li$_{2.9}$Ca$_y$Ba$_{0.05-y}$PS$_4$; conductivities at 300 K and activation energies of Li$_{3-2x}$Ca$_x$PS$_4$ and Li$_{2.9}$Ca$_y$Ba$_{0.05-y}$PS$_4$; deconvolved results of ^{31}P and ^{7}Li

MAS NMR spectra for $Li_{3-2x}Ca_xPS_4$ and $Li_{2.9}Ca_yBa_{0.05-y}PS_4$; and illustrations of optimized crystal structures for $Li_{3-2x}Ca_xPS_4$ obtained by DFT (PDF)

■ AUTHOR INFORMATION

Corresponding Author

Takahiro Ohkubo − *Graduate School of Engineering, Chiba University, Chiba 263-8522, Japan;* ● orcid.org/0000-0001-8187-1470; Phone: +81 (0)43 2903435; Email: ohkubo.takahiro@faculty.chiba-u.jp; Fax: +81 (0) 43 2903431

Authors

Fuki Baba − *Graduate School of Engineering, Chiba University, Chiba 263-8522, Japan*

Futoshi Utsuno − *Lithium Battery Material Department, Idemitsu Kosan Co., Ltd., Chiba 299-0293, Japan*

Complete contact information is available at:
https://pubs.acs.org/10.1021/acsomega.3c09952

Notes

The authors declare no competing financial interest.

■ REFERENCES

(1) Janek, J.; Zeier, W. G. A solid future for battery development. *Nat. Energy* **2016**, *1*, 16141.

(2) Lee, Y.-G.; Fujiki, S.; Jung, C.; Suzuki, N.; Yashiro, N.; Omoda, R.; Ko, D. S.; Shiratsuchi, T.; Sugimoto, T.; Ryu, S.; et al. High-energy long-cycling all-solid-state lithium metal batteries enabled by silver−carbon composite anodes. *Nat. Energy* **2020**, *5*, 299−308.

(3) Fan, L.-Z.; He, H.; Nan, C.-W. Tailoring inorganic−polymer composites for the mass production of solid-state batteries. *Nat. Rev. Mater.* **2021**, *6*, 1003−1019.

(4) Zheng, F.; Kotobuki, M.; Song, S.; Lai, M. O.; Lu, L. Review on solid electrolytes for all-solid-state lithium-ion batteries. *J. Power Sources* **2018**, *389*, 198−213.

(5) Zhang, Q.; Cao, D.; Ma, Y.; Natan, A.; Aurora, P.; Zhu, H. Sulfide-based solid-state electrolytes: synthesis, stability, and potential for all-solid-state batteries. *Adv. Mater.* **2019**, *31*, 1901131.

(6) Nolan, A. M.; Zhu, Y.; He, X.; Bai, Q.; Mo, Y. Computation-Accelerated Design of Materials and Interfaces for All-Solid-State Lithium-Ion Batteries. *Joule* **2018**, *2*, 2016−2046.

(7) Huang, Y.; Shao, B.; Han, F. Interfacial challenges in all-solid-state lithium batteries. *Curr. Opin. Electrochem.* **2022**, *33*, 100933.

(8) Li, C.; Wang, Z.-y.; He, Z.-j.; Li, Y.-j.; Mao, J.; Dai, K.-h.; Yan, C.; Zheng, J.-c. An advance review of solid-state battery: Challenges, progress and prospects. *Sustainable Mater.Technol.* **2021**, *29*, No. e00297.

(9) Goodenough, J.; Hong, H.-P.; Kafalas, J. Fast Na⁺-ion transport in skeleton structures. *Mater. Res. Bull.* **1976**, *11*, 203−220.

(10) Feng, J. K.; Yan, B. G.; Liu, J. C.; Lai, M. O.; Li, L. All solid state lithium ion rechargeable batteries using NASICON structured electrolyte. *Mater. Technol.* **2013**, *28*, 276−279.

(11) Latie, L.; Villeneuve, G.; Conte, D.; Le Flem, G. Ionic conductivity of oxides with general formula $Li_xLn_{1/3}Nb_{1-x}Ti_xO_3$ (Ln = La, Nd). *J. Solid State Chem.* **1984**, *51*, 293−299.

(12) Chen, C.; Xie, S.; Sperling, E.; Yang, A.; Henriksen, G.; Amine, K. Stable lithium-ion conducting perovskite lithium-strontium-tantalum-zirconium-oxide system. *Solid State Ionics* **2004**, *167*, 263−272.

(13) Kuwano, J.; West, A. New Li⁺ ion conductors in the system, Li_4GeO_4-Li_3VO_4. *Mater. Res. Bull.* **1980**, *15*, 1661−1667.

(14) Bruce, P.; West, A. Ionic conductivity of LISICON solid solutions, $Li_{2+2x}Zn_{1-x}GeO_4$. *J. Solid State Chem.* **1982**, *44*, 354−365.

(15) Geiger, C. A.; Alekseev, E.; Lazic, B.; Fisch, M.; Armbruster, T.; Langner, R.; Fechtelkord, M.; Kim, N.; Pettke, T.; Weppner, W. Crystal Chemistry and Stability of "$Li_7La_3Zr_2O_{12}$" Garnet: A Fast Lithium-Ion Conductor. *Inorg. Chem.* **2011**, *50*, 1089−1097.

(16) Banerjee, A.; Wang, X.; Fang, C.; Wu, E. A.; Meng, Y. S. Interfaces and interphases in all-solid-state batteries with inorganic solid electrolytes. *Chem. Rev.* **2020**, *120*, 6878−6933.

(17) Wang, C.; Adair, K. R.; Liang, J.; Li, X.; Sun, Y.; Li, X.; Wang, J.; Sun, Q.; Zhao, F.; Lin, X.; et al. Solid-state plastic crystal electrolytes: effective protection interlayers for sulfide-based all-solid-state lithium metal batteries. *Adv. Funct. Mater.* **2019**, *29*, 1900392.

(18) Yu, C.; Zhao, F.; Luo, J.; Zhang, L.; Sun, X. Recent development of lithium argyrodite solid-state electrolytes for solid-state batteries: Synthesis, structure, stability and dynamics. *Nano Energy* **2021**, *83*, 105858.

(19) Arnold, W.; Buchberger, D. A.; Li, Y.; Sunkara, M.; Druffel, T.; Wang, H. Halide doping effect on solvent-synthesized lithium argyrodites Li_6PS_5X (X = Cl, Br, I) superionic conductors. *J. Power Sources* **2020**, *464*, 228158.

(20) Park, K. H.; Bai, Q.; Kim, D. H.; Oh, D. Y.; Zhu, Y.; Mo, Y.; Jung, Y. S. Design strategies, practical considerations, and new solution processes of sulfide solid electrolytes for all-solid-state batteries. *Adv. Energy Mater.* **2018**, *8*, 1800035.

(21) Lu, X.; Xia, G.; Lemmon, J. P.; Yang, Z. Advanced materials for sodium-beta alumina batteries: Status, challenges and perspectives. *J. Power Sources* **2010**, *195*, 2431−2442.

(22) Tachez, M.; Malugani, J.-P.; Mercier, R.; Robert, G. Ionic conductivity of and phase transition in lithium thiophosphate Li_3PS_4. *Solid State Ionics* **1984**, *14*, 181−185.

(23) Homma, K.; Yonemura, M.; Kobayashi, T.; Nagao, M.; Hirayama, M.; Kanno, R. Crystal structure and phase transitions of the lithium ionic conductor Li_3PS_4. *Solid State Ionics* **2011**, *182*, 53−58.

(24) Liu, Z.; Fu, W.; Payzant, E. A.; Yu, X.; Wu, Z.; Dudney, N. J.; Kiggans, J.; Hong, K.; Rondinone, A. J.; Liang, C. Anomalous high ionic conductivity of nanoporous β-Li_3PS_4. *J. Am. Chem. Soc.* **2013**, *135*, 975−978.

(25) Hayashi, A.; Hama, S.; Morimoto, H.; Tatsumisago, M.; Minami, T. Preparation of Li_2S−P_2S_5 Amorphous Solid Electrolytes by Mechanical Milling. *J. Am. Ceram. Soc.* **2001**, *84*, 477−479.

(26) Thangadurai, V.; Narayanan, S.; Pinzaru, D. Garnet-type solid-state fast Li ion conductors for Li batteries: critical review. *Chem. Soc. Rev.* **2014**, *43*, 4714−4727.

(27) Hamabe, K.; Utsuno, F.; Ohkubo, T. Lithium conduction and the role of alkaline earth cations in Li_2S-P_2S_5-MS (M = Ca, Sr, Ba) glasses. *J. Non-Cryst. Solids* **2020**, *538*, 120025.

(28) Zhou, L.; Assoud, A.; Shyamsunder, A.; Huq, A.; Zhang, Q.; Hartmann, P.; Kulisch, J.; Nazar, L. F. An Entropically Stabilized Fast-Ion Conductor: $Li_{3.25}[Si_{0.25}P_{0.75}]S_4$. *Chem. Mater.* **2019**, *31*, 7801−7811.

(29) Zhang, Z.; Li, H.; Kaup, K.; Zhou, L.; Roy, P.-N.; Nazar, L. F. Targeting superionic conductivity by turning on anion rotation at room temperature in fast ion conductors. *Matter* **2020**, *2*, 1667−1684.

(30) Adeli, P.; Bazak, J. D.; Huq, A.; Goward, G. R.; Nazar, L. F. Influence of aliovalent cation substitution and mechanical compression on Li-ion conductivity and diffusivity in argyrodite solid electrolytes. *Chem. Mater.* **2021**, *33*, 146−157.

(31) Moon, K.; Lee, H. J.; Park, K. H.; Kwak, H.; Heo, J. W.; Choi, K.; Yang, H.; Kim, M. S.; Hong, S. T.; Lee, J. H.; Jung, Y. S. Vacancy-Driven Na⁺ Superionic Conduction in New Ca-Doped Na_3PS_4 for All-Solid-State Na-Ion Batteries. *ACS Energy Lett.* **2018**, *3*, 2504−2512.

(32) Doebelin, N.; Kleeberg, R. Profex: a graphical user interface for the Rietveld refinement program BGMN. *J. Appl. Crystallogr.* **2015**, *48*, 1573−1580.

(33) Kresse, G.; Hafner, J. Ab initio molecular dynamics for liquid metals. *Phys. Rev. B: Condens. Matter Mater. Phys.* **1993**, *47*, 558−561.

(34) Blöchl, P. E. Projector augmented-wave method. *Phys. Rev. B: Condens. Matter Mater. Phys.* **1994**, *50*, 17953−17979.

(35) Perdew, J. P.; Burke, K.; Ernzerhof, M. Generalized Gradient Approximation Made Simple. *Phys. Rev. Lett.* **1996**, *77*, 3865−3868.

(36) Monkhorst, H. J.; Pack, J. D. Special points for Brillouin-zone integrations. *Phys. Rev. B: Condens. Matter Mater. Phys.* **1976**, *13*, 5188−5192.

(37) Grimme, S.; Antony, J.; Ehrlich, S.; Krieg, H. A consistent and accurate ab initio parametrization of density functional dispersion correction (DFT-D) for the 94 elements H-Pu. *J. Chem. Phys.* **2010**, *132*, 154104.

(38) Lepley, N. D.; Holzwarth, N. A. W.; Du, Y. A. Structures, Li^+ mobilities, and interfacial properties of solid electrolytes Li_3PS_4 and Li_3PO_4 from first principles. *Phys. Rev. B: Condens. Matter Mater. Phys.* **2013**, *88*, 104103.

(39) Yang, Y.; Wu, Q.; Cui, Y.; Chen, Y.; Shi, S.; Wang, R.-Z.; Yan, H. Elastic properties, defect thermodynamics, electrochemical window, phase stability, and Li^+ mobility of Li_3PS_4: Insights from first-principles calculations. *ACS Appl. Mater. Interfaces* **2016**, *8*, 25229−25242.

(40) Stöffler, H.; Zinkevich, T.; Yavuz, M.; Senyshyn, A.; Kulisch, J.; Hartmann, P.; Adermann, T.; Randau, S.; Richter, F. H.; Janek, J.; et al. Li^+-ion dynamics in β-Li_3PS_4 observed by NMR: local hopping and long-range transport. *J. Phys. Chem. C* **2018**, *122*, 15954−15965.

(41) Momma, K.; Izumi, F. VESTA 3 for three-dimensional visualization of crystal, volumetric and morphology data. *J. Appl. Crystallogr.* **2011**, *44*, 1272−1276.

(42) Primak, W.; Kaufman, H.; Ward, R. X-ray diffraction studies of systems involved in the preparation of alkaline earth sulfide and selenide phosphors1. *J. Am. Chem. Soc.* **1948**, *70*, 2043−2046.

(43) Hadenfeldt, C.; Hoedel, D. Kristallstruktur und Eigenschaften von Calcium- und Strontiumhexathiodiphosphat(IV), $Ca_2P_2S_6$ und $Sr_2P_2S_6$, mit einem Beitrag zu Ca_5P_8 und $Pb_2P_2S_6$. *Z. Anorg. Allg. Chem.* **1996**, *622*, 1495−1500.

(44) Rad, H. D.; Hoppe, R. Über Thiomercurate. 2. Zur Kenntnis von Ba_2HgS_3. *Z. Anorg. Allg. Chem.* **1981**, *483*, 7−17.

(45) Jörgens, S.; Mewis, A.; Hoffmann, R.-D.; Pöttgen, R.; Mosel, B. D. Neue Hexachalcogeno-Hypodiphosphate der Erdalkalimetalle und des Europiums. *Z. Anorg. Allg. Chem.* **2003**, *629*, 429−433.

(46) Eckert, H.; Zhang, Z.; Kennedy, J. H. Structural transformation of non-oxide chalcogenide glasses. The short-range order of lithium sulfide (Li_2S)-phosphorus pentasulfide (P_2S_5) glasses studied by quantitative phosphorus-31, lithium-6, and lithium-7 high-resolution solid-state NMR. *Chem. Mater.* **1990**, *2*, 273−279.

(47) Kudu, Ö. U.; Famprikis, T.; Cretu, S.; Porcheron, B.; Salager, E.; Demortiere, A.; Courty, M.; Viallet, V.; Mercier, T. L.; Fleutot, B.; Braida, M.-D.; Masquelier, C. Structural details in Li_3PS_4: Variety in thiophosphate building blocks and correlation to ion transport. *Energy Storage Mater.* **2022**, *44*, 168−179.

(48) Dietrich, C.; Weber, D. A.; Sedlmaier, S. J.; Indris, S.; Culver, S. P.; Walter, D.; Janek, J.; Zeier, W. G. Lithium ion conductivity in Li_2S−P_2S_5 glasses building units and local structure evolution during the crystallization of superionic conductors Li_3PS_4, $Li_7P_3S_{11}$ and $Li_4P_2S_7$. *J. Mater. Chem. A* **2017**, *5*, 18111−18119.

(49) Stöffler, H.; Zinkevich, T.; Yavuz, M.; Hansen, A.-L.; Knapp, M.; Bednarčík, J.; Randau, S.; Richter, F. H.; Janek, J.; Ehrenberg, H.; Indris, S. Amorphous versus Crystalline Li_3PS_4: Local Structural Changes during Synthesis and Li Ion Mobility. *J. Phys. Chem. C* **2019**, *123*, 10280−10290.

(50) Zhao, P.; Boekfa, B.; Nishitoba, T.; Tsunoji, N.; Sano, T.; Yokoi, T.; Ogura, M.; Ehara, M. Theoretical study on ^{31}P NMR chemical shifts of phosphorus-modified CHA zeolites. *Microporous Mesoporous Mater.* **2020**, *294*, 109908.

(51) Kirkpatrick, R. J.; Brow, R. K. Nuclear magnetic resonance investigation of the structures of phosphate and phosphate-containing glasses: a review. *Solid State Nucl. Magn. Reson.* **1995**, *5*, 9−21.

(52) Gobet, M.; Greenbaum, S.; Sahu, G.; Liang, C. Structural evolution and Li dynamics in nanophase Li_3PS_4 by solid-state and pulsed-field gradient NMR. *Chem. Mater.* **2014**, *26*, 3558−3564.

(53) Carta, D.; Knowles, J. C.; Smith, M. E.; Newport, R. J. Synthesis and structural characterization of P_2O_5-CaO-Na_2O sol-gel materials. *J. Non-Cryst. Solids* **2007**, *353*, 1141−1149.

(54) Cherbib, M. A.; Khattech, I.; Montagne, L.; Revel, B.; Jemal, M. Structure properties relationship in calcium sodium metaphosphate and polyphosphate glasses. *J. Non-Cryst. Solids* **2018**, *485*, 1−13.

(55) Cherbib, M. A.; Krimi, S.; El Jazouli, A.; Khattech, I.; Montagne, L.; Revel, B.; Jemal, M. Structure and thermochemical study of strontium sodium phosphate glasses. *J. Non-Cryst. Solids* **2016**, *447*, 59−65.

(56) Hayamizu, K.; Aihara, Y. Lithium ion diffusion in solid electrolyte $(Li_2S)_7(P_2S_5)_3$ measured by pulsed-gradient spin-echo ^7Li NMR spectroscopy. *Solid State Ionics* **2013**, *238*, 7−14.

(57) Uchida, K.; Ohkubo, T.; Utsuno, F.; Yazawa, K. Modified $Li_7P_3S_{11}$ glass-ceramic electrolyte and its characterization. *ACS Appl. Mater. Interfaces* **2021**, *13*, 37071−37081.

(58) Fischer, M.; Evers, F. O.; Formalik, F.; Olejniczak, A. Benchmarking DFT-GGA calculations for the structure optimization of neutral-framework zeotypes. *Theor. Chem. Acc.* **2016**, *135*, 257.

(59) Charpentier, T.; Ispas, S.; Profeta, M.; Mauri, F.; Pickard, C. J. First-principles calculation of ^{17}O, ^{29}Si, and ^{23}Na NMR spectra of sodium silicate crystals and glasses. *J. Phys. Chem. B* **2004**, *108*, 4147−4161.

(60) Fang, H.; Jena, P. Argyrodite-type advanced lithium conductors and transport mechanisms beyond paddle-wheel effect. *Nat. Commun.* **2022**, *13*, 2078.

(61) Rangasamy, E.; Wolfenstine, J.; Sakamoto, J. The role of Al and Li concentration on the formation of cubic garnet solid electrolyte of nominal composition $Li_7La_3Zr_2O_{12}$. *Solid State Ionics* **2012**, *206*, 28−32.

(62) Bernstein, N.; Johannes, M. D.; Hoang, K. Origin of the Structural Phase Transition in $Li_7La_3Zr_2O_{12}$. *Phys. Rev. Lett.* **2012**, *109*, 205702.